Volume 14
Number 14
3 March 2026
Pages 7829–8416

Journal of Materials Chemistry A

Materials for energy and sustainability

rsc.li/materials-a

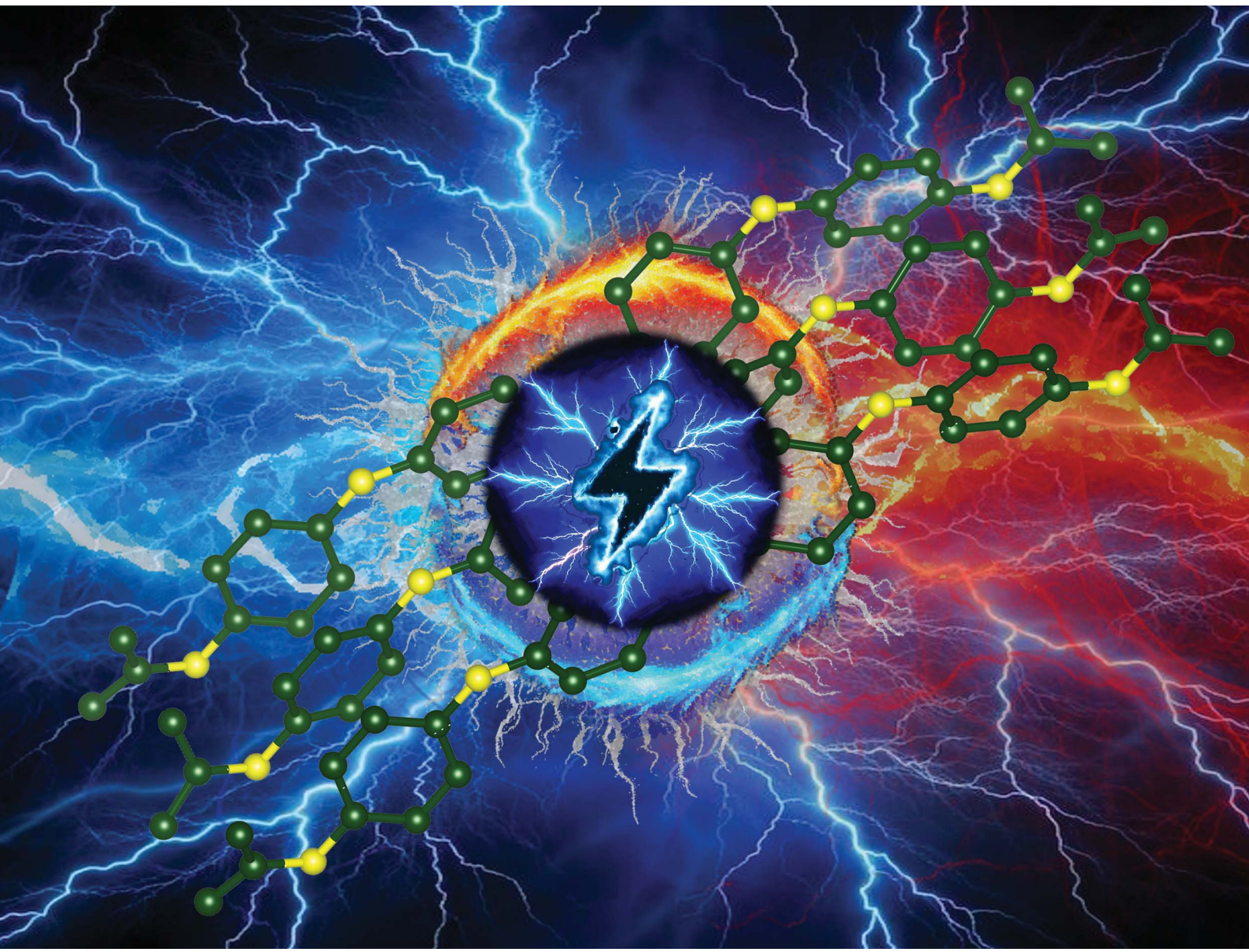

ISSN 2050-7488

ROYAL SOCIETY OF CHEMISTRY

PAPER

Nagendra Singh Chauhan, Takao Mori *et al.*
Energy filtering and anisotropic structural response in polyaniline:CSA hybrids for flexible thermoelectrics

Journal of Materials Chemistry A

ROYAL SOCIETY OF CHEMISTRY

PAPER

View Article Online
View Journal | View Issue

Cite this: J. Mater. Chem. A, 2026, 14, 8014

Energy filtering and anisotropic structural response in polyaniline:CSA hybrids for flexible thermoelectrics

Anmol Sharma, [ab] Nagendra Singh Chauhan *[a] and Takao Mori *[ab]

Recent advances in polymer nanocomposites have opened promising routes for engineering carrier characteristics, phonon dynamics and conformational disorders, paving the way for next-generation thermoelectric materials. Herein, we report the development of free-standing, flexible films of $Mg_{0.99}Cu_{0.01}Ag_{0.97}Sb_{0.99}$ nanofiller-incorporated PANI:CSA polymer nanocomposites. The hybrid nanocomposites showed nearly a tenfold increase in the power factor and Seebeck coefficient, accompanied by a synergistic reduction (~100%) in thermal conductivity, yielding a thermoelectric figure of merit (zT) of ~0.13 (±0.02) at ~300 K. Transport analysis employing the Kang–Snyder (KS) framework and Semi-Localized Transport (SLoT) modeling reveals an invariant scattering exponent in the semi-localized regime, implying preserved diffusive polaronic transport, improved interfacial connectivity, and energy-filtering-driven mobility enhancement, while structural and spectroscopic analyses reveal anisotropic lattice adaptation, dedoping-induced polaron stabilization, bond charge distribution, and preserved pseudo-orthorhombic order in PANI. To validate its practical applicability, a flexible thermoelectric generator was fabricated, producing an output voltage of ~11.6 mV and underscoring the promise of Te-free, interface-engineered polymer–inorganic hybrids for wearable energy harvesting.

Received 6th November 2025
Accepted 30th December 2025

DOI: 10.1039/d5ta09036a

rsc.li/materials-a

1 Introduction

The growing global demand for sustainable energy, coupled with the vast amounts of low-grade waste heat dissipated from the human body, portable devices, and ambient environments, has fueled interest in exploring a TE pathway toward self-powered flexible and wearable electronics.[1–4] In this regard, conducting polymers have emerged as attractive candidates for thermoelectric (TE) energy harvesting owing to their intrinsic flexibility, low density, and thermal conductivity (κ), along with moderate electrical conductivity (σ) and excellent processability in solution.[5–7] Amongst technologically relevant polymers, polyaniline (PANI) in particular, stands out due to its environmental stability, redox reversibility, and stable π-conjugated structure. Interestingly, their electrical properties are tunable over a remarkably wide range (from insulating to metallic-like), which controls the balance of polaron (singly charged, spin – 1/2) and bipolaron (doubly charged, spin – 0) species along the conjugated backbone.[8–10] However, PANI and other organic thermoelectrics are limited by their inherently low Seebeck coefficients (S) and moderate electrical conductivity (σ), as increasing carrier density (n) broadens the transport energy distribution and suppresses S (a classic S–σ trade-off that constrains TE performance).[11,12]

Interestingly, hybrid composite strategies integrate conducting polymers with inorganic nanostructures (such as Te,[13] Bi_2Te_3,[14,15] and SnSeS[16]) and carbon-based materials (such as graphene and CNTs) to combine complementary advantages, where the polymer matrix provides mechanical compliance and low κ, while inorganic and carbon-based fillers provide percolation pathways, energy filtering effects, and carrier localization and scattering to decouple inverse S–σ interdependence.[17,18] For instance, ternary hybrid systems combining PANI with carbon nanotubes and inorganic nanostructures such as PANI/MWCNT/Te-NRs,[19] PANI/SWCNT/Te-NRs,[20] PANI/a-CNT/TiO_2,[21] and PANI/$CuSbSe_2$/MWCNT,[22] have been reported with low Seebeck values in the range of ≈20–60 μV K^{-1} through controlled doping/oxidation, chain alignment, and interfacial energy filtering strategies.[16,20–26] However, these values remain far below those of inorganic thermoelectrics (several hundred μV K^{-1}), significantly limiting their practical efficiency. While nanocomposites like PANI-Te/Se have shown modest improvements,[13,16] and CNT-based conductive scaffolds[27] show high power factors ($S^2\sigma$), achieving precise Seebeck tunability has remained challenging due to inherent charge transport limitations in the polymer matrix.

In our recent work,[28] we demonstrated that charge localization (*via* suppression of bipolarons) in PANI/ZnSb composite

[a]Research Center for Materials Nanoarchitectonics (MANA), National Institute for Materials Science (NIMS), Namiki 1-1, Tsukuba, 305-0044, Japan. E-mail: CHAUHAN.NagendraSingh@nims.go.jp; MORI.Takao@nims.go.jp

[b]Graduate School of Pure and Applied Sciences, University of Tsukuba, 1-1-1 Tennodai, Tsukuba, Ibaraki 305-8573, Japan

films can enhance the Seebeck coefficient. Herein, by blending high TE performance *p*-type fillers with intrinsically low lattice thermal conductivity (κ_L) and a high Seebeck coefficient[29,30] *i.e.* the $Mg_{0.99}Cu_{0.01}Ag_{0.97}Sb_{0.99}$ (hereafter referred to as MACS) filler into the conducting PANI matrix, this study aims to achieve flexible, *p*-type PANI:CSA/MACS (hereafter denoted as PMACS) hybrid nanocomposites capable of efficient utilization of low-grade heat. Varying MACS contents (*i.e.*, 20–70 wt%) synergize charge carrier localization[28] and energy filtering[20,26] at the interfaces, which increases the Seebeck coefficient up to ~76 μV K^{-1} at ~300 K, and ~99 μV K^{-1} at ~373 K corresponding to a high zT ~ 0.13 at ~300 K for PMACS70. To elucidate the composite's structure and chemical interactions, variations in the electron density function across the polymer unit cell with different inorganic fillers underscore the coupled effects of chain alignment and interfacial charge transfer, resulting in anisotropic structural response upon MACS intercalation in PANI-based hybrids. The Raman, XPS, and UV-vis-NIR analyses reveal conformational reorganization, polaron localization, and de-doping effects at the PANI/MACS interface, while Hall measurement results *i.e.* increasing carrier mobility (μ) and decreasing carrier concentration (n), corroborate well with inferences of carrier energy filtering. The transport analysis conducted by using the Kang–Snyder[31] and the Semi-Localized Transport (SLOT)[32] framework, reveals spatial localization and enhanced interconnectivity at interfaces. To demonstrate practical feasibility, a prototype flexible thermoelectric generator (FTEG) based on the PANI/MACS composite was fabricated, showing reliable power output from small temperature gradients and highlighting its potential for wearable energy applications.

2 Results and discussion

2.1 Retention of the crystallographic framework and anisotropic structural response

The crystalline domains of PANI:CSA in its emeraldine salt (ES) form is a semi-crystalline conjugated polymer, where order arises mainly from the π–π stacking of phenyl rings and periodicity along the polymer backbone.[28,33] The XRD diffraction pattern shown in Fig. 1(a) exhibits broad reflection at around 22–24°, indexed as the (112) plane, corresponding to π–π interchain stacking of phenyl rings, while the peak at ~9–11° corresponds to the periodic distance between polymer backbones in the semi-crystalline domains. At low filler loadings, only the amorphous or semi-crystalline polymer's XRD signals were visible, while with increasing filler loading, the filler aggregation, phase separation, or crystallization, albeit within the matrix, lead to pronounced XRD peaks for the α-MgAgSb crystalline ($I\bar{4}c2$, 120) phase.[34] Remarkably, CSA doping induces a highly ordered extended coil conformation in PANI chains, which provides stability against structural collapse when MACS fillers are added. Thus, the lattice planes in refinements were essentially the same as presented in SI Fig. S3–S9. The Rietveld refinement parameters considering the pseudo-orthorhombic phase (space group: *Pc*2*a*, 32) are listed in Table S1.[35,36] For high MACS content, expansion is so extensive resulting in exfoliated nanocomposites, wherein regular layered order disappears, and new diffraction peaks corresponding to crystalline α-MgAgSb phases were observed as a dominant peak. As the concentration of the inorganic filler increases, its diffraction peak becomes stronger and easier to identify in the XRD profile.

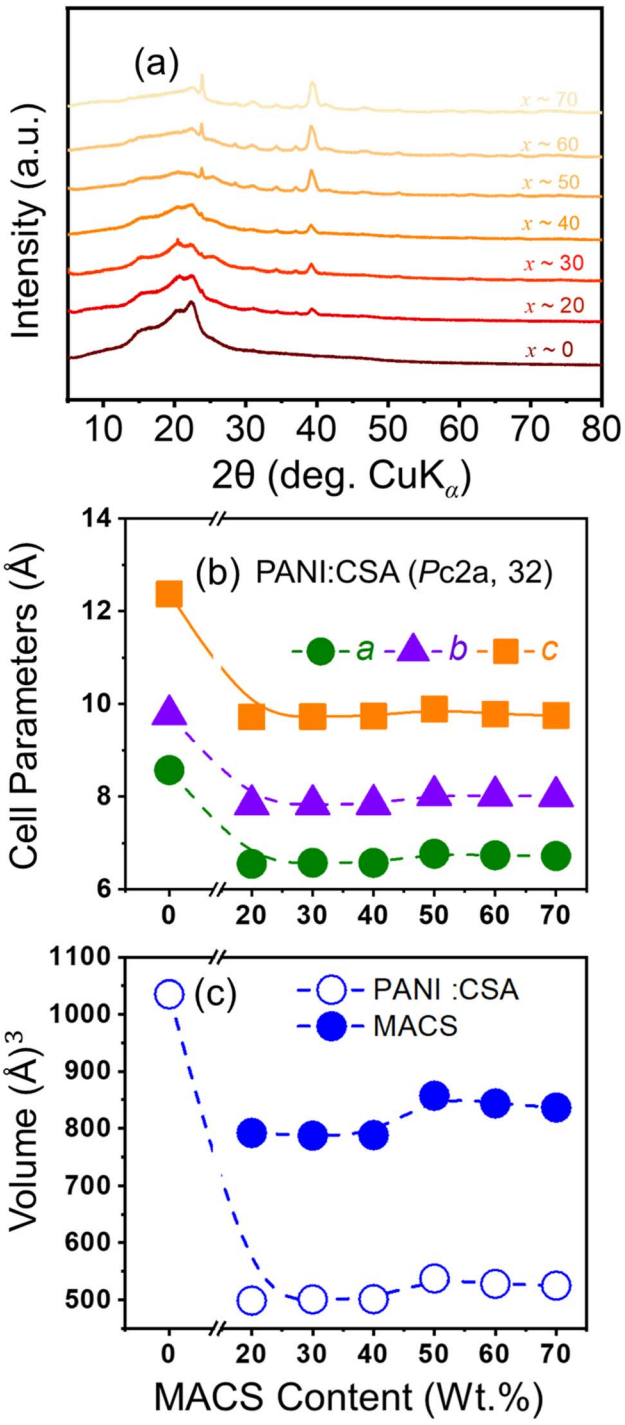

Fig. 1 (a) X-ray diffraction patterns of PMACS (0–70%) hybrid nanocomposite films, (b) refined lattice parameters for pseudo-orthorhombic PANI:CSA complex unit cells, (c) unit cell volume of MACS fillers and the PANI:CSA matrix, and varying MACS content in the synthesized PANI:CSA/MACS nanocomposite.

Interestingly, MgAgSb is a thermoelectric filler which exhibits intrinsic cation disorder and vacancy tolerance.[34] The α-MgAgSb unit cell presented in Fig. S2 indicates marginal changes, with expansion of the *c*-axis for higher MACS content, suggesting filler interaction with the polymeric chain. Upon hybridization/intercalation, a shift to lower angles (implying expanded periodicity) and an increased *d*-spacing for (010) and (101), presumably reflect inter-chain expansion caused by MACS insertion or polymer–filler hybridization. Thus, MACS fillers intercalate within PMACS, and interact with chains, but they do not disrupt the fundamental ordering motif of PANI chains (*i.e.*, the planes such as (112), (200), (022), (210), *etc.*), shifting them to higher angles, indicating contraction in π–π stacking and conjugation along the polymer backbone upon blending with inorganic MACS fillers. As filler inclusion does not strongly perturb the π orbitals (HOMO–LUMO levels) of PANI:CSA, hybridization likely promotes energy filtering (interface scattering) rather than new hybrid orbital formation. Even though

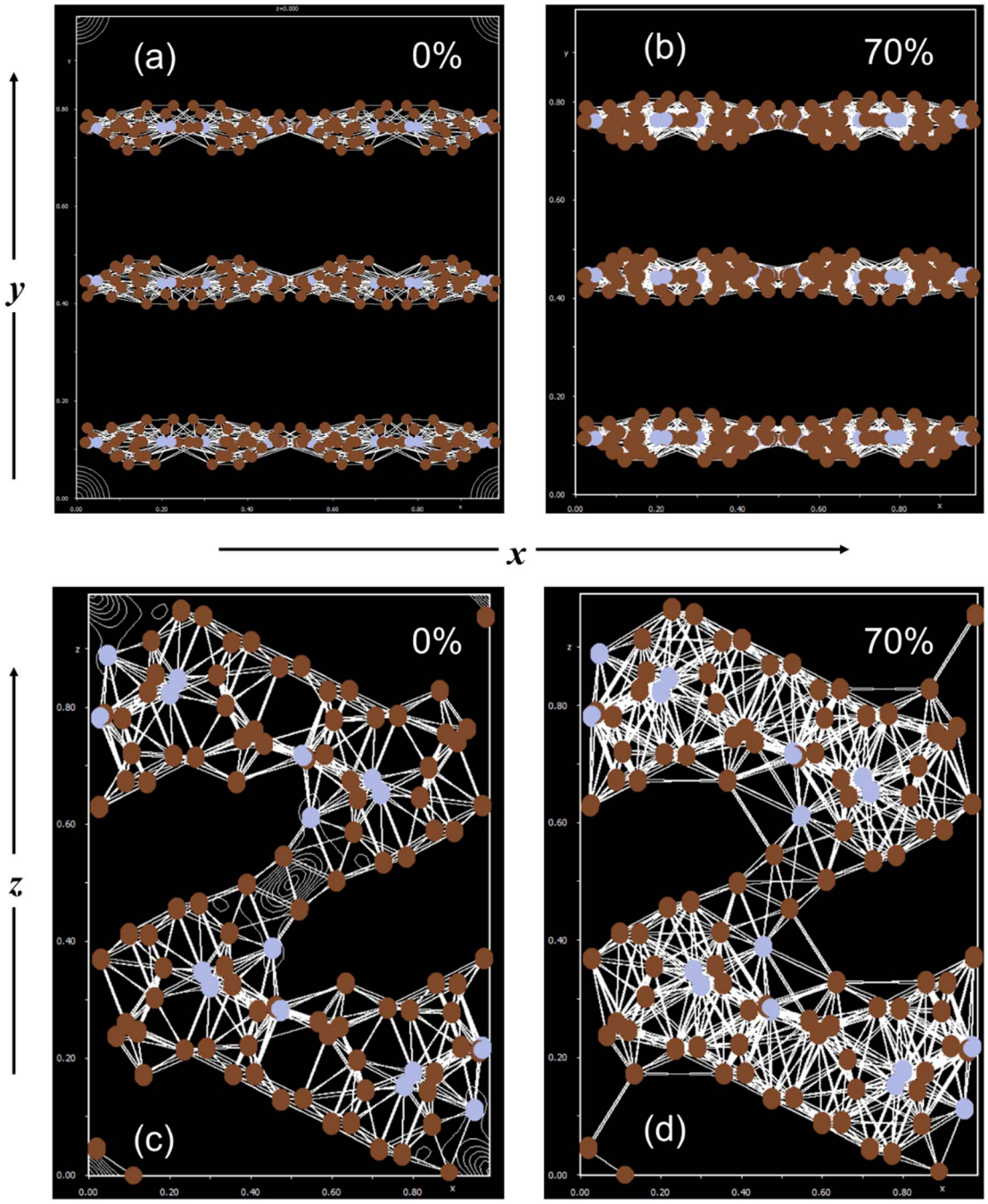

Fig. 2 Spatial probability represented by the electron density function distribution of the PANI:CSA unit cell in synthesized (a and c) pristine PANI:CSA showing contours within the polymer chain, indicative of enhanced electronic delocalization; and (b and d) PMACS70 displaying increased electron density along the bond axes, suggesting stronger and more localized bonding interactions.

similar planes are indexed and the inter-planar distances expand, the lattice parameter decreases significantly in PMACS and varies marginally with increasing MACS content as shown in Fig. 1(b). The overall lattice contraction (smaller *a*, *b*, or *c* parameters after refinement) suggests that beyond the local intercalation zones, the remaining crystalline domains compact. This happens because filler inclusion may introduce electrostatic interactions, or partial crosslinking between PANI chains, with improved orbital overlap.

Unlike inorganic crystals, MACS does not elastically strain the PANI lattice; rather, it perturbs the packing of PANI chains, CSA dopants, and microcrystalline lamellae. The MACS fillers apparently modify packing anisotropically: along the chain direction by promoting extended conformations or partial alignment, and perpendicular to the chains by locally increasing inter-chain separation through CSA intercalation, trapped species, or MACS–PANI interfacial regions. Essentially, local expansion near interfaces coexists with global densification of the crystal framework as also presented by volumetric changes in PANI:CSA and MACS with increasing content. The lattice contraction despite the peak shift suggests that hybridization induces localized intercalation and interfacial reorganization with contraction rather than global swelling, leading to internal densification while preserving the basic crystallographic framework of PANI:CSA. Volumetric changes in PANI–filler hybrids are direct structural signatures of polymer–filler interaction strength, chain rearrangement, and charge transfer at the interface. From Rietveld refinement, the unit cell volume (*V*) is determined from lattice parameters (*a*, *b*, and *c*) and is shown in Fig. 1(c). In PMACS, contraction of unit cell volume and shift of diffraction maxima to higher angles (lower *d*-spacing) suggest interchain compaction and enhanced crystallinity. Strong electrostatic or hydrogen-bond interactions between filler surface atoms (*e.g.*, Sb and Mg^{2+}) and PANI's –NH– or $–N^+$ sites may increase crystallinity and interchain alignment. The MACS filler apparently acts as a nucleation center, improving structural order (reflected in sharper XRD peaks), while strong interfacial charge coupling causes PANI chains to reorganize into denser conformations, stabilizing bipolarons as also observed and discussed in XPS results.

2.2 Molecular configuration, improved conjugation and morphology of flexible films

The electron density function within the polymer unit cell provides a quantitative visualization of charge distribution and bonding character to better understand electronic localization/delocalization and structural organization. Fig. 2 presents the difference Fourier map representing the residual electron density, wherein continuous contours along the backbone were observed in protonated PANI, indicating electron delocalization along conjugated chains. In pristine PANI, the electron density shown in Fig. 2(a and c) is primarily concentrated along the π-conjugated backbone (C=C and C–N bonds) and between benzenoid and quinoid rings, corresponding to delocalized π-electrons responsible for electrical transport. With MACS intercalation as presented in Fig. 2(b and d), electronic coupling (*e.g.*, hybridization between polymer N 2p and filler metal s/p orbitals) and ionic interactions manifest as changes in XRD Fourier maps, showing denser contours around filler-coordinated atoms and along the backbone direction. Upon introducing inorganic fillers, a sustained crystallographic framework with high inter-chain *vs.* intra-chain electron distribution, implying strong covalent or π-bonding interactions is obtained.

The density and continuity of contours between atoms directly reflect the strength and nature of bonding, wherein denser, multiple contours were evaluated for PMACS, indicating stronger, localized covalent bonds, compared to the more spread-out contours indicative of delocalized electrons for protonated PANI:CSA. The electron density maps along the backbone, showing dense contours connecting neighboring carbon or heteroatoms, suggest strong covalent bonds, indicating weak charge transfer or dipole–dipole coupling between PANI and the inorganic species. This typically enhances local polarization and may create shallow trap states, and slightly modify the potential landscape, but retains overall π-conjugation continuity. The strong polarization gradients and spatially separated domains suggest that fillers induce charge confinement or potential wells, which influence the density of states near the Fermi level. This restructuring can lead to charge carrier suppression/localization, enhanced energy filtering, and a shift in the transport mechanism from extended-state conduction to hopping-type transport (Mott or ES-VRH). Thus, intercalation in MgAgSb–polymer hybrids expands lattice spacing and provides new charge pathways, while steric effects from bulky polymer chains induce strain, reduce crystallinity, and alter phonon/electron scattering.

SEM analysis reveals distinct differences between pristine PANI:CSA and PANI/MACS70 composite films (Fig. 3). The pristine PANI:CSA surface [Fig. 3(a)] appears comparatively uniform and featureless, without any cracks and pores, indicative of a densely packed polymer layer with minimal surface irregularities. By contrast, the PANI/MACS70 film [Fig. 3(b)] shows a heterogeneous surface comprising granular domains and clustered inorganic particles interconnected within the polymer matrix. At this loading, MACS particles appear partially wrapped by PANI layers, as suggested by polymer-smoothed particle contours, consistent with the development of a percolated microstructure at high filler content, and consistent with the morphologies widely observed in polymer-inorganic TE composites at high loadings.[7,13,15,28,37] Elemental mapping (Fig. 3(c)–(j)) verifies the presence and distribution of both the polymer and filler constituents. The elemental signals corresponding to Mg, Ag, Cu, and Sb align with the inorganic phase, while C, N, and S arise from the PANI backbone and CSA dopant. Notably, the polymer elements are also detected on MACS-rich regions, in line with interfacial wrapping of PANI around the filler. This interfacial morphology, together with the relatively uniform element distributions, underscores the effectiveness of the sequential stirring–ultrasonication route in promoting good mixing and suppressing large-scale phase separation. Cross-sectional SEM images [Fig. 3(k) and (l)] reveal thicknesses of ~41 μm for pristine PANI:CSA and ~58 μm for

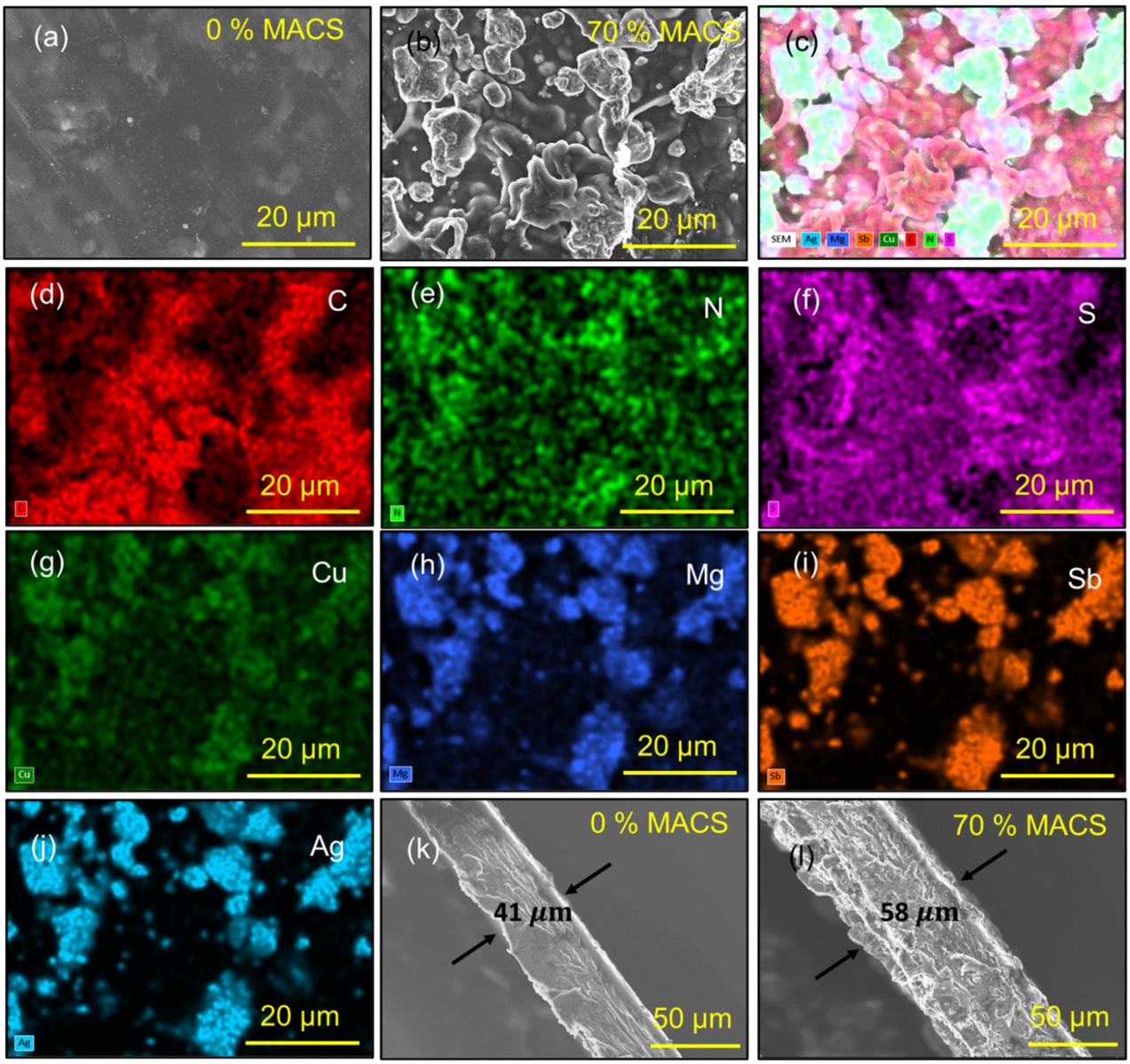

Fig. 3 SEM micrographs illustrate (a) the PANI:CSA film and (b) granular morphology of embedded MACS clusters in the PMACS70 nanocomposite film. (c–j) EDX elemental mapping of the region shown highlights the distinct distribution of MACS clusters within the polymeric PANI matrix. Cross-sectional SEM image of (k) PANI:CSA & (l) PMACS70, respectively.

the PANI/MACS70 film. The increase in film thickness with a higher filler fraction may be attributed to the larger inorganic content, which increases rigidity and modifies film packing. Notably, both pristine and composite films remain intact and free of cracks, even at 70 wt% MACS loading, reflecting their mechanical resilience and suitability for flexible device fabrication.

2.3 Reduced protonation efficiency and chain conformation changes

Raman spectroscopy was performed to characterize interactions between PANI:CSA and MACS and analyze the molecular structure, conjugation, and doping levels. Fig. 4(a) shows the stacked Raman spectra of PANI:CSA and PMACSx composite films ($x \sim$ 20–70 wt%), wherein the PANI:CSA film exhibits all the characteristic vibrational bands expected for that of well-doped polyaniline. In the low-frequency region, modes appear at ~414 and 515 cm^{-1}, corresponding to out-of-plane deformations in the PANI base,[8,9] whereas peaks at 579, 716, and 812 cm^{-1} are assigned to phenazine-type cross-linking,[38,39] ring deformation in the PANI base,[8,40,41] and benzene ring distortions,[9,39] respectively. Following MACS incorporation, the peaks corresponding to out-of-plane deformations in the PANI matrix were blue-shifted to 418 and 521 cm^{-1}, indicating a restriction of these motions. This observation aligns with SEM images showing PANI layers wrapping over the MACS grains. Additionally, the peak at 414 cm^{-1} splits into two distinct peaks at 418 and 437 cm^{-1}, likely reflecting the presence of different

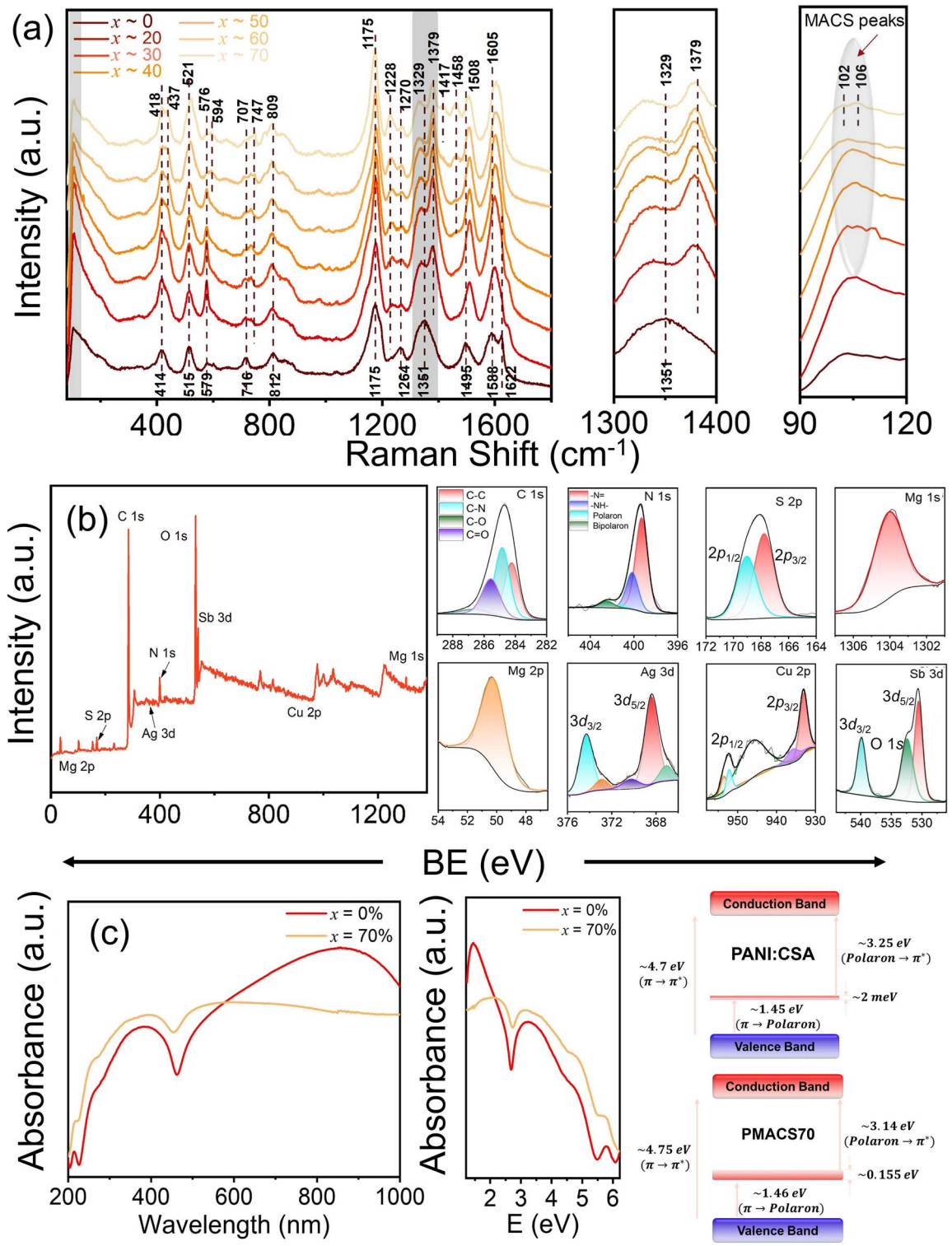

Fig. 4 (a) Raman spectra of PMACS (0–70%), (b) XPS wide-scan survey spectra and high-resolution elemental spectra of PMACS70, and (c) UV-vis-NIR spectra of the PANI:CSA and PMACS70 nanocomposite films.

aromatic cycles, as reported by Colomban *et al.*[8] The peak at 579 cm^{-1} is red-shifted to 576 cm^{-1}, and an extra peak appears at 594 cm^{-1} in PMACS70, which is consistent with phenazine-like crosslinking and restricted phenylene torsions within the PANI rings.[8] The peak at 716 cm^{-1} also red-shifts to 707 cm^{-1}, accompanied by new features at 730 cm^{-1}, 747 cm^{-1}, and 780 cm^{-1} in PMACS70, which can be attributed to ring deformations and phenazine-like crosslinks in the emeraldine base.[39] The peak at 812 cm^{-1} is red-shifted to 809 cm^{-1}, which is attributed to benzene ring distortions in PANI salt, while the

appearance of a peak at 851 cm^{-1} in PMACS70 corresponds to an out-of-plane C–C deformation of quinonoid rings, consistent with quinonoid enrichment and crosslinking at higher filler content.[39,40]

In the higher frequency region, PANI:CSA exhibits prominent peaks at 1175, 1264, 1351, 1495, 1588, and 1622 cm^{-1}, characteristic of the emeraldine salt form. These can be assigned to C–H deformation vibrations of quinonoid (QN)/semi-quinoid (SQN) units, C–N stretching vibrations in QN structures, $C–N^{+\bullet}$ stretching modes of the SQN cation radicals in delocalized polaronic structures, N–H deformations in the SQN units, C–C stretching vibrations of the SQN ring, and C–C stretching modes of the benzenoid (BZ) ring.[9] Increasing the MACS filler content induces systematic shifts in peak positions and substantial intensity changes, evidencing strong polymer–filler interactions and modification of PANI's chemical structure. Notably, the high-frequency band at 1622 cm^{-1} markedly decreases in intensity and undergoes a blue shift with increasing MACS loading, and subsequently vanishes in the PMACS70 composite film, indicating the reduced doping level, as also observed by Lindfors *et al.*;[42] with the increase in pH (basicity) in PANI, no characteristic benzenoid peak at 1622 cm^{-1} was observed. This suggests a conversion of BZ rings to QN rings, and a loss of some protonated imine sites at higher MACS content, consistent with the reduced doping level in the polymer. The peak at 1588 cm^{-1} is blue-shifted to 1605 cm^{-1} along with an increase in its intensity, indicating the structural modification of QN structures, as observed previously.[43,44] The peak near 1495 cm^{-1} for PANI:CSA is shifted to 1508 cm^{-1} for PMACS70, along with a slight increase in its intensity, which arises from coupled semi-quinoid N–H deformations with C=N stretching that is highly sensitive to oxidation/(de)protonation and local coordination.[43–46]

Two more peaks emerge at 1458 cm^{-1} and 1417 cm^{-1} (not seen in PANI:CSA), attributed to C=N stretching modes in QN rings, and C–N stretching vibrations in highly localized polaronic structures, respectively. These peaks are assumed to be consistent with interfacial stiffening at N-sites, slight deprotonation, and polaron localization with increased imine character as previously observed in PANI salts.[40,41,45,47] The peak at 1351 cm^{-1} ($C–N^{+\bullet}$ vibrations of the SQN cations in delocalized polaronic structures) for PANI:CSA is shifted to 1329 cm^{-1} for the PMACS70 sample with a decrease in its intensity, indicating decreased delocalization of polarons. Apart from this peak, a shoulder peak at 1379 cm^{-1} also emerges after MACS incorporation, which is attributed to $C–N^{+\bullet}$ stretching modes in highly localized polarons (this peak is not visible in PANI:CSA). The intensity of this peak is increased with increasing MACS content and overshadows the peak at 1329 cm^{-1}. This suggests the presence of highly localized polaronic states, which may trap the polarons (charge carriers) and impede their transport. In contrast, the delocalized polaronic structures are decreased, which may lead to a decrease in carrier concentration & electrical conductivity, but an enhancement in the Seebeck coefficient.[28,39,40,48]

The 1264 cm^{-1} band (C–N stretching vibration in QN structures/polaronic unit)[46] in PANI:CSA shifts to ~1270 cm^{-1} at MACS70 loading, accompanied by a significant decrease in its intensity, and splits into another peak at 1228 cm^{-1} corresponding to C–N stretching modes in BZ rings, which emerges and overshadows the 1270 cm^{-1} band with increasing MACS loading up to 70 wt%, and is known to grow upon deprotonation towards the EB state, exactly what interfacial coordination with MACS can induce. This C–N splitting clearly separates QN from BZ units.[46,48] The growth of this peak at ~1228 cm^{-1} suggests the chemical structure shift towards the EB-state with deprotonated states (since the PANI-EB form contains both C=N and C–N bonds), as also inferred by Lindfors *et al.*[42] who ascribed the peak at ~1221 cm^{-1} for a higher pH PANI (which was absent in lower pH PANI), and also observed fading away of the peak at ~1253 cm^{-1} due to overlapping by 1221 cm^{-1}. This peak is accompanied by another peak at ~1477 cm^{-1} (C=N stretching vibration of QN rings). In our PMACS70 films, both C=N and C–N bonds are observed, indicating a chemical structure shift toward the emeraldine base (EB) form upon MACS incorporation. The band at 1175 cm^{-1}, corresponding to C–H bending of quinoid (QN) rings, retains its position even at 70 wt% MACS loading, but shows a slight increase in intensity, consistent with a modest increase in QN/SQN segments.[46,48]

In addition to the high-frequency modifications, new low-frequency modes emerge in the composites below 150 cm^{-1}, which are absent in pure PANI:CSA. These low-energy bands can be assigned to lattice vibrations of the MgAgCuSb phase and potential polymer–filler interfacial phonon modes. Their appearance indicates that the MACS filler introduces additional vibrational degrees of freedom into the system, in line with previous reports showing that Cu/Sb-based inclusions alter the phonon spectrum of Mg–Ag compounds.[30] The observation of these new modes, together with shifts in PANI's backbone vibrations (*e.g.*, shifts in the 1622, 1588, 1495, 1351, 1264, 1175, 812, 716, 579, 515, and 414 cm^{-1} bands), corroborates strong chemical interactions between PANI chains and the dispersed MACS filler particles.

2.4 Coordinated chemical and electronic reorganization

The "coordinated chemical and electronic reorganization" of PANI is the synchronous tuning of backbone chemistry, dopant structure, and charge carrier distribution, which together control its crystalline order, density of states, and transport properties. X-ray photoelectron spectroscopy (XPS), shown in Fig. 4(b) reveals a coordinated chemical and electronic reorganization of polyaniline upon incorporation of 70 wt% MACS. The high-resolution elemental XPS spectra (C, N, and S) of PANI:CSA are shown in Fig. S11. This reorganization is evidenced by shifts in binding energies and changes in peak intensities, reflecting modifications in the oxidation states, protonation levels, and local electronic environment of the polymer chains. A wide survey scan shows the presence of expected elements (C, N, O, and S from PANI:CSA; and Mg, Ag, Cu, Sb from MACS), consistent with the successful formation and interaction between PANI:CSA and MACS. Although the signal for Cu 2p was very low and negligible during the wide survey scan, this may be due to its low stoichiometry in MACS and low

sweep times during the scan. But during the high-resolution elemental scan with high sweep and scan time, the Cu 2p spectra could be obtained.

The high-resolution N 1s spectrum of the PANI:CSA film (Fig. S11) reveals four distinct components, corresponding to different nitrogen environments in the PANI salt form, *i.e.*, imine (=N–, quinoid-imine), amine (–NH–, benzenoid-amine), polaron, and bipolaron, corresponding to the peak position at 399.1 eV, 400.2 eV, 401.6 eV, and 403.4, respectively, in line with prior PANI-based literature.[23,28,49–52] The presence of polarons and bipolarons is a signature of the delocalized and protonated form of PANI upon CSA doping.[28,51] Upon PMACS-70 incorporation, the same nitrogen species are shifted to 399.3 eV, 400.2 eV, 401.3 eV, and 402.5 eV, respectively, with their respective changes in areal concentration shown in Table S2. The imine fraction increased from 48.48% to 66.52%, while the polaron fraction decreased from 15.10% to 2.18%; the bipolaron fraction remained the same, and the overall charged-nitrogen content (polaron + bipolaron) fell from 20.37% to 7.44%, while the neutral nitrogen content (imine + amine) increased from 79.62% to 92.56%. Concomitantly, the polaron and bipolaron binding energies shifted to lower values by 0.3 eV and 0.9 eV, respectively, indicating greater electron density screening around the remaining charged nitrogen, consistent with lower net protonation and strong coordination with N-sites. In contrast, the amine component remained unchanged, and the imine peak shifted slightly to higher energy (0.2 eV). These changes signify pronounced deprotonation/EB-like character and stabilization of neutral imine units at the PANI/MACS interface, with strong suppression of polaronic charge and a small residual bipolaron signature indicating the charge localization induced by MACS incorporation.[28,52] The N 1s trends are fully consistent with Raman spectroscopy (growth of the 1228 and 1379 cm^{-1} bands; loss of the 1622 cm^{-1} benzenoid band), UV-vis spectroscopy (weakened NIR polaron tail, explained below), and transport ($\mu_H\downarrow$, $\sigma\downarrow$, and $S\uparrow$), evidencing deprotonation/de-doping, and charge carrier localization, induced by the MACS filler.

The high-resolution C 1s spectrum reveals four different carbon components in PANI:CSA (Fig. S11), corresponding to C–C/C=C (aromatic ring carbon), C–N/C=N (carbon atoms adjacent to amine, imine, and charged nitrogen), C–O, and C=O (both are oxidized carbonyl species), with their respective peaks at 284.3 eV, 285.3 eV, 286.7 eV, and 287.9 eV, which are consistent with the previously reported literature.[51,53,54] With the incorporation of MACS, the peaks for the respective C 1s components are shifted to 284.2 eV, 284.8 eV, 285.6 eV, and 286.7 eV, as shown in Table S2. In C 1s, the spectral weight transfers from C–C (62.33 → 31.62)% to heteroatom-bound carbon (C–N: 25.92% → 38.03%, C–O: 8.60% → 25.27%, C=O: 3.15% → 5.08%) with all heteroatom components shifting to lower BE, consistent with loss of C–N^+ character and interfacial coordination that increases electron density on N/O-bearing carbons, and growth of neutral imine/amine character (EB-like), as has been seen in several PANI composites,[28,53–55] together with electron-richer O-bound carbon which may be produced by oxidation or interfacial coordination/screening at MACS.[7,50,52] In addition, the relative fraction of C–O/C=O is increased by ~3 times in the PMACS70 composite, indicating the hydrolysis and oxidation of the composite film, which may also be due to the reactive nature of conjugated polymers, and the film peeling process in DI water, as Mg is very sensitive to water.[51,53] These trends are consistent with PANI:CSA layers wrapping MACS grains.

The high-resolution S 2p spectrum is attributed to the doping of CSA (SO_4^{2-}). For PANI:CSA (Fig. S11), the peaks at 167.5 eV and 168.8 eV correspond to $2p_{3/2}$ and $2p_{1/2}$ with a ΔB.E. ≈ 1.3 eV, while for PMACS70, the peaks at 167.8 eV and 169 eV correspond to $2p_{3/2}$ and $2p_{1/2}$ with a ΔB.E. ≈ 1.2 eV, coming within the –SO_3^- (sulfonate/sulfate) range and far above reduced S (161–165 eV), confirming that sulfur derives exclusively from CSA and retains S(VI).[7,53,54] Relative to PANI:CSA, the composite shows a uniform +0.2–0.3 eV upshift without line-shape change, indicating no redox change, but a modified local electrostatic environment. We attribute this to weaker electrostatic pairing with N^+ (N 1s de-doping) together with weak coordination of SO_3^- oxygens to MACS surface cations, which may slightly withdraw electron density from the sulfonate and increase the B.E., consistent with the polymer-MACS hybrid.[7,28,53,54,56,57] The Mg 1s maximum is at 1304.0 eV and Mg 2p at 50.3 eV which sit above metallic Mg (≈1303 and 49.8 eV), placing Mg in a Mg^{2+} state, indicating the presence of MgO/$Mg(OH)_2$. The symmetric line shapes and absence of low BE-shoulders exclude residual Mg^0.

The assignment is consistent with MACS hybrids where Mg 1s ≈ 1306 and 1304 eV directly indicate Mg^{2+} at the surface, and these small positive BE offsets *vs.* standards arise from the mild oxidation and inter-element interactions.[7,58] The Ag 3d doublet at 368.4 eV ($3d_{5/2}$) and 374.3 eV ($3d_{3/2}$) with a B.E. ≈ 5.9 eV, matches Ag in MACS and metallic Ag references, indicating an oxidation state of Ag^{1+},[7] while a weak component at ~367.0 eV indicates Ag oxide; the shoulders at ~370.2 eV and 372.9 eV are inelastic losses, and are not used for chemical quantification.[7,59] The high-resolution Cu 2p spectrum shows $2p_{3/2}$ at 933.1 eV and $2p_{1/2}$ at 952.7 eV, with a clear ~945.7 eV shake-up satellite, evidencing a minor Cu^{2+} surface fraction on a Cu^+-dominated lattice (evident by the $2p_{3/2}$ peak). The peak at ~936.6 eV feature belongs to the Cu^{2+} satellite/multiplet region rather than a distinct chemical state.[7,49,60] The high-resolution Sb 3d spectrum reveals a doublet, *i.e.*, $3d_{5/2}$ ~ 530.5 eV and $3d_{3/2}$ ~ 539.9 eV, with a spin–orbit splitting of ~9.4 eV. Originally, the Sb $3d_{5/2}$ peak exists near 328 eV, but a shift to 530.5 eV and a superimposed O 1s (at ~532.4 eV) peak with $3d_{5/2}$ suggest the formation of an antimony oxide (Sb_2O_3) phase, and the oxidation state of Sb^{3+}.[7,49]

2.5 Dedoping tendency and charge localization

The UV-vis-NIR spectra of pristine $PMACS_x$ (x = 0%) and $PMACS_x$ (x = 70%) films, shown in Fig. 4(c) reveal systematic modifications in the electronic transitions upon incorporation of the MACS inorganic filler. For pristine PANI:CSA, the characteristic $\pi \rightarrow \pi^*$ transition of the benzenoid rings is centered at ~264 nm (~4.70 eV), the polaron → π^* transition at

~382 nm (~3.25 eV), and the broad π → polaron band extends into the NIR with a maximum near 856 nm (~1.45 eV). After MACS incorporation, the π → π* band undergoes a slight hypsochromic shift to 261 nm (~4.75 eV) with reduced intensity, indicating a shortened effective conjugation length and partial loss of chain planarization.[52,61] In the deep-UV region, the band at 215 nm, probably arising from residual *m*-cresol, shifts marginally to 217 nm with decreased absorbance, consistent with perturbed benzenoid electronic transitions and modified counter-ion environments at the polymer–filler interface.[61]

Interestingly, after MACS incorporation, the π → polaron transition blue-shifts slightly from 856 to 851 nm (1.46 eV) while its intensity is strongly suppressed. This behavior is a well-established fingerprint of reduced polaronic/bipolaronic delocalization, as previously reported for de-doped PANI and low-doping regimes in CNT/PANI composites.[23,61] In contrast, systems that enhance delocalization through secondary doping or π–π interactions with graphene exhibit a strengthened and red-shifted NIR tail.[52,62] Thus, MACS incorporation drives the electronic structure towards localized polaron states rather than extended delocalization, lowering conductivity. The polaron → π* band shifts from 382 to 395 nm (~3.14 eV), a red shift that reflects altered polaron binding energies and interfacial perturbation of the electronic coupling between the PANI backbone and its charged species. Such red shifts of the polaron → π* absorption are also reported in partial de-doping–re-doping sequences where localization effects dominate.[23,28] Mapping these transitions onto the energy level diagram places the polaron ~1.45 eV & ~1.46 eV above the valence band for PANI:CSA & PMACS70 films, respectively, but shows a reduced polaron → conduction band (≈0.11 eV) in PMACS70, *i.e.*, the polaron level lies slightly closer to the conduction band while the overall π → π* edge hardens marginally (with a blue shift).[63] Quantitatively, the absorbance ratio, A(395)/A(851), is increased markedly in PMACS, providing an optical metric that tracks the $\sigma\downarrow/S\uparrow$ trade-off expected from charge carrier localization/energy filtering mechanisms.[28,61]

Taken together, these spectral modifications, suppression of the NIR band, the red-shifted polaron → π* transition, and the blue-shifted π → π* transition build a coherent picture of interfacial charge localization in PANI chains embedded within MACS. This localization is also corroborated by Raman and XPS analyses, which show the suppression of polarons and partial deprotonation of imine sites. From a thermoelectric perspective, such localization is beneficial for increasing the Seebeck coefficient along with energy filtering effects while concurrently reducing electrical conductivity, a trade-off also noted in prior studies of charge-localized PANI films,[28] and observed from the Hall measurements as explained below. Importantly, the opposite trend is observed when conductive carbon fillers or Bi_2Te_3 nanoparticles are introduced, which narrows the optical bandgap and strengthens long-wavelength absorption.[64] Therefore, the UV-vis spectra confirm that MACS acts not as a delocalization agent but as a localization driver, stabilizing polarons in more confined states and thereby rationalizing the observed enhancement in thermopower of PMACS composites. Thus, the spectrum resembles that of partially de-doped PANI, lying between the emeraldine salt and emeraldine base forms. The suppressed long wavelength absorption band indicates a shift in the transport mechanism toward localized polarons with hopping-like conduction. As a result, polarons lose their delocalization, leading to reduced electrical conductivity.

2.6 Chain conformation strategy for conductivity and thermopower enhancement

Conductivity in polymers such as PANI is strongly dependent on the chain conformation adopted in the solid state, wherein the arrangement of the polymer backbone, the degree of planarity, and the inter-chain interactions govern both the extent of π-electron delocalization and the efficiency of charge transport.[28] To optimize the intrinsic conductivity of PANI:CSA, we employed a sequential stirring–ultrasonication protocol during film preparation, aimed at minimizing chain agglomeration and promoting extended-chain conformations of PANI:CSA in *m*-cresol.[65–67] Consistent with the observations of MacDiarmid *et al.*[68,69] extended coil-like conformation/stretching in PANI significantly enhances electrical conductivity. This extended geometry promotes planarization of the polymer backbone, enabling stronger π–π orbital overlap between adjacent chains.

In the current approach, cycles of 10 min of stirring followed by 10 min ultrasonication were repeated for 1 h, yielding well-dispersed solutions with minimal chain entanglement and enhanced charge delocalization. This resulted in protonated PANI:CSA films with an intrinsic room-temperature conductivity of ≈ 298 S cm^{-1}, representing a significant improvement over our previous report[28] (≈170 S cm^{-1} for films prepared without this chain-conformation strategy) and surpassing the typical literature range of 100–200 S cm^{-1} for PANI:CSA.[70–72] A schematic of the fabrication process for PANI:CSA/MACS composites is shown in SI Fig. S1. The resulting free-standing films exhibit excellent mechanical flexibility and remain crack-free even at high filler loadings of up to 70 wt%. The enhancement arises from the unique role of m-cresol as a secondary dopant, which promotes coil-to-extended chain transformation of PANI. Through strong interactions with both the $-SO_3^-$ groups of CSA and the protonated $-NH_3^+$ sites of the polymer backbone[67], m-cresol facilitates chain planarization, improved π–π stacking, and enhanced interchain connectivity. When coupled with ultrasonication, these interactions are further reinforced, leading to superior chain ordering and an interconnected transport network.[65,66]

2.7 Temperature-dependent electrical properties

The thermoelectric properties of PANI:CSA and PMACS$_x$ (x ≈ 20–70 wt%) composites were measured in the temperature range between 297 and 373 K. Fig. 5(a) shows the temperature dependence of the electrical conductivity, $\sigma(T)$, for pristine PANI:CSA and PMACS composites (20–70 wt%). At 300 K, the pristine film exhibits $\sigma \approx 295$ S cm^{-1}, consistent with a highly ordered, conformed, and protonated emeraldine-salt network that contains quasi-metallic pathways.[73] With increasing MACS content, the electrical conductivity falls monotonically,

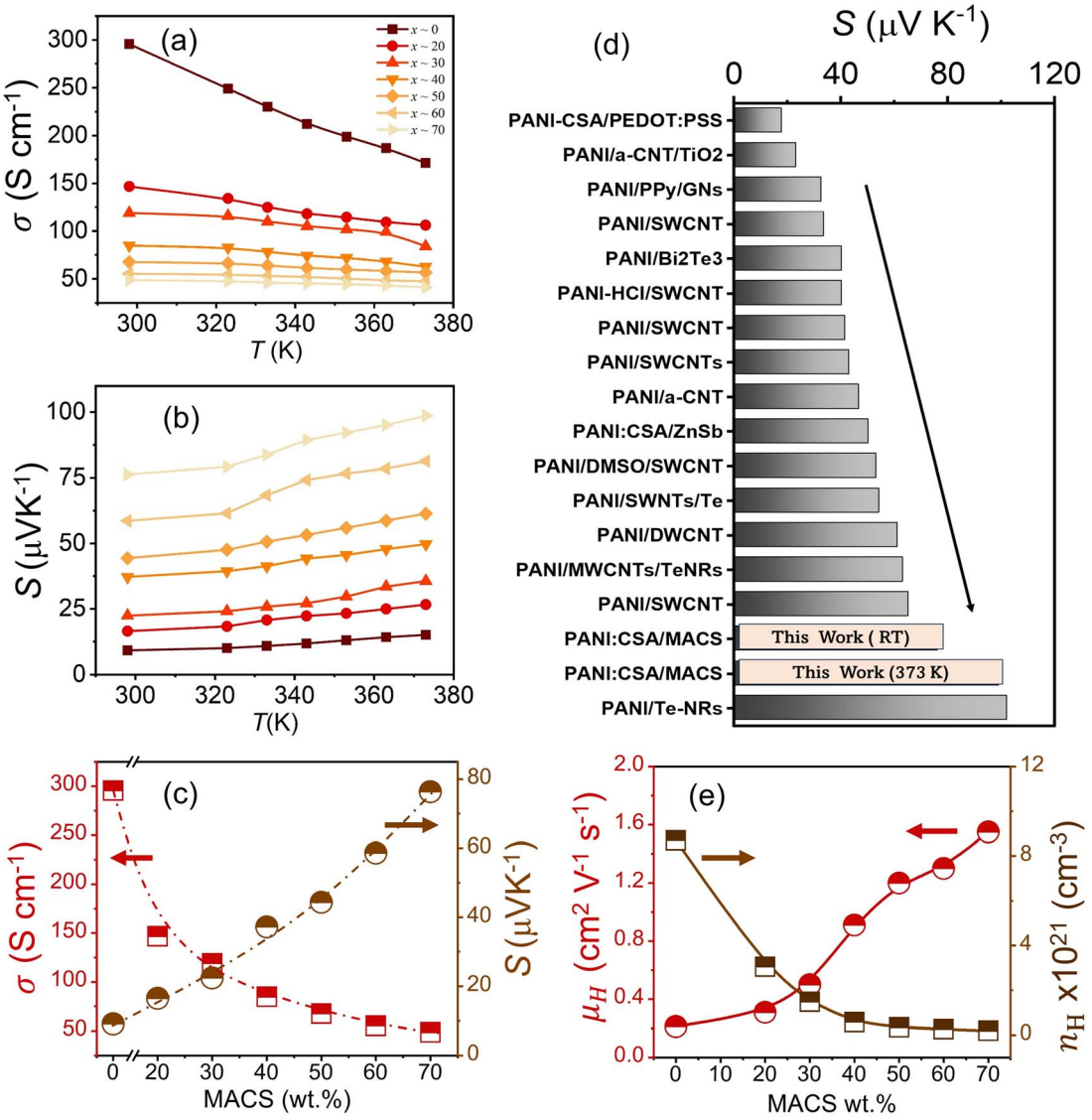

Fig. 5 Temperature dependence of (a) electrical conductivity and (b) Seebeck coefficient of the PMACS (0–70 wt%) hybrid nanocomposite; (c) electrical conductivity and Seebeck coefficient of the PMACS hybrid nanocomposite at room temperature as a function of MACS content; (d) state-of-the art comparison of the Seebeck coefficient achieved in PANI-based composites; (e) carrier concentration and mobility as a function of MACS content obtained from room-temperature Hall measurements.

reaching $\sigma \approx 50$ S cm^{-1} at $x \approx 70$ wt%. For all compositions, $\sigma(T)$ shows a weakly negative slope ($d\sigma/dT < 0$) across 300–380 K, indicating thermally activated scattering within a disordered polaronic manifold. This behavior is ascribed to a degenerate semiconductor or a dirty metal, possessing quasi-metallic conduction pathways.[28,73–76] The overall σ decreases with MACS which reflects two concurrent effects established earlier by spectroscopy: (i) carrier localization owing to polaron suppression and partial deprotonation (evident de-doping),[28,75,76] and (ii) interfacial barriers at polymer–MACS contacts that impede low-energy carriers.[20–22] Both mechanisms diminish the effective dc carrier population contributing to transport, shifting the films away from the quasi-degenerate limit observed in pristine PANI:CSA. Furthermore, to identify the charge transport mechanism underlying this $\sigma(T)$ behavior, we next analyze it with a hopping framework.[77,78] Both Mott-VRH and Efros–Shklovskii VRH (ES-VRH) fits were employed to understand the nature of carrier hopping between localized states as presented in SI Fig. S15 and discussed in S3.1. Since the PANI matrix in these flexible composites exhibits strong electronic disorder and inter-site Coulomb interactions at moderate doping, the Efros–Shklovskii (ES) VRH model provides a more physically meaningful description than Mott-VRH, capturing the Coulomb-gap–limited hopping behavior that dominates in such localized polaronic systems. The temperature dependent ES-VRH model fitting of electrical conductivity with a negative temperature exponent of −1/2 demonstrates linear behavior as shown in Fig. S16. The ES-VRH model has been further explained in SI Section S7.1.

Fig. 5(b) presents the Seebeck coefficient $S(T)$, which is positive for all the films, confirming p-type polaron conduction. At room temperature (~300 K), pristine PANI:CSA yields $S \approx 10$

$\mu V\ K^{-1}$, which increases steadily with MACS loading, reaching $\sim$76 $\mu V\ K^{-1}$ for the PMACS-70 film, which may be ascribed to charge carrier localization and energy filtering effects with increasing MACS content, as becomes evident from spectroscopic studies and Hall measurements, and further analyzed by KS and SLoT models (as presented in the next section). With temperature, $S(T)$ increases monotonically with increasing temperature for every composition. For the PMACS70 composition, the $S(T)$ increases from $\sim$76 $\mu V\ K^{-1}$ to $\sim$99 $\mu V\ K^{-1}$ from RT to 373 K. This monotonic increase in $S(T)$, *i.e.*, dS/dT, can be attributed to reduced carrier concentration due to carrier scattering *via* MACS particles, and charge carrier localization. These linear-like increases in $S(T)$ are consistent with the Mott relation for disordered semiconductors, as validated by Watanabe *et al.*,[79] which is given by

$$S \propto m^* T \left(\frac{1}{n}\right)^{2/3}$$

where m^*, n, and T denote the charge effective mass, carrier concentration, and temperature, respectively. This equation predicts that S will increase with incresing temperature and decrease with increasing carrier concentration, which is the trend observed in our PANI/MACS system. As shown in Fig. 5(d), previously reported S is typically tens of $\mu V\ K^{-1}$ but some PANI/CNT composites reach $\geq$50 $\mu V\ K^{-1}$ at an optimized composition or temperature. The measured S is comparable to the highest reported values for PANI composites,[13] validating the structural and doping characteristics achieved and influencing energy filtering and carrier scattering at the nanoscale. Mechanical flexibility and performance stability were further confirmed through bending tests, demonstrating sustained TE output after approximately 2000 bending cycles (Fig. S13).

2.8 Tunable thermopower, an enhanced power factor and thermal conductivity reduction

The high conductivity obtained for PANI:CSA is particularly significant in the context of polymer–inorganic hybrids, where S enhancement is often offset by a loss in σ due to the intrinsic σ–S trade-off as shown in Fig. 5(c). An inverse and composition-dependent relationship between the S and σ for PANI:CSA/MACS films ($\sim$300–380 K), with a steady climb in S and a fall in σ from pristine PANI:CSA can be seen as MACS content increases.[28] Each composition traces an up-right locus with increasing temperature: $\sigma(T)$ decreases while $S(T)$ increases, consistent with a degenerate (near metallic region) regime.[73,76] Establishing a strong baseline conductivity buffers the polymer matrix against this penalty, and enables the incorporation of high-Seebeck fillers such as MACS without severe conductivity loss, as a second step towards enhanced performance. In addition, interfacial energy filtering can selectively promote the transport of high-energy carriers, further sustaining charge mobility while boosting S, and charge carrier localization (suppression of polarons/bipolarons), indicative of charge carrier confinement, which can trap the charge carriers and may lead to enhanced S.[20–23,28] This dual advantage, elevated intrinsic σ and interfacial energy-filtering/charge-carrier localization, provides a favorable platform for simultaneously enhancing both σ and S, or lowering the rate of decrease in σ, thereby unlocking synergistic improvements in the power factor ($S^2\sigma$). Unlike prior PANI hybrids, where conductivity degradation constrained net gains, this work illustrates how careful control of polymer chain morphology and dispersion can shift the balance toward improved electrical contribution to thermoelectric efficiency, without using CNTs.

The room temperature Hall measurement results are presented in Fig. 5(e), showing carrier concentration (n_H) and carrier mobility (μ_H). A pronounced anti-correlation is observed between n_H and μ_H, where n_H decreases by nearly an order of magnitude from $x = 0$ to 70 wt% MACS, while μ_H increases from $\sim$0.2 to $\sim$1.5 $cm^2\ V^{-1}\ s^{-1}$. Since $\sigma = ne\mu$, the decline in the n_H explains the decrease in σ. Physically, this trend arises from interfacial energy filtering at PANI/MACS interfaces, where low-energy carriers are scattered (decreasing n_H) while allowing high-energy carriers to pass through, resulting in increased mobility with MACS. Comparable anti-correlation in n_H and μ_H with a concurrent increase in S has been observed in several PANI systems, *i.e.*, PANI:CSA/BST[15] and PANI/MWCNT/Te,[19] consistent with an interfacial energy-filtering barrier that scatters low-energy carriers[19–23,51] Nearly an order-of-magnitude decrease in n_H across 0 to 70 wt% MACS accompanied by a moderate increase in μ_H, indicates that the carriers that do conduct are higher-energy, more selectively transmitted, and a hallmark of interfacial energy filtering operating alongside charge carrier localization in PANI hybrids.[19–22]

The temperature dependent power factors for PANI:CSA and PMACS nanocomposite films are presented in Fig. 6(a). For all compositions, the PF increases with T, driven by a monotonic increase in $S(T)$ that outweighs the decline in $\sigma(T)$. At 300 K, PF increases from $\approx$ 3 $\mu W\ m^{-1}\ K^{-2}$ (PANI:CSA) to $\approx$ 30 $\mu W\ m^{-1}\ K^{-2}$ (PMACS70). For the PMACS70 film, the PF reaches $\approx$40 $\mu W\ m^{-1}\ K^{-2}$ near 373 K. This $\sim$10 times enhancement in the PF is attributed to an increased Seebeck coefficient (charge localization & energy filtering effect), enabling a strategy towards obtaining a higher Seebeck coefficient and PF in polymeric systems for flexible, Te/Se-free hybrid TE materials. Thermal stability of the PMACS70 sample was evaluated by TGA (Fig. S14a), with detailed analysis provided in Supplementary Section S6. Fig. 6(b) presents the temperature-dependent thermal conductivity (κ) of pristine PANI and the optimized PMACS70 nanocomposite, calculated from temperature-dependent thermal diffusivity (D) and specific heat capacity (C_p) data shown in Fig. S14(b) and (c). Consistent with the amorphous polymer network dominated by phonon scattering at chain boundaries and disordered segments, pristine PANI exhibits a low $\kappa \approx 0.15\ W\ m^{-1}\ K^{-1}$ at 300 K, consistent with the previous report.[27] Upon incorporation of nanoscale MACS fillers, the thermal conductivity shows significant decrement within the range of 0.06–0.07 $W\ m^{-1}\ K^{-1}$ at $\sim$300 K. Here, the electrical and thermal conduction for PANI:CSA is occurring *via* the polaronic mechanisms as the polarons are delocalized and coupled with the lattice that take part in thermal conduction. But for PMAC70, the polarons are either trapped or localized, so thermal energy is primarily dominated by phonons, which is

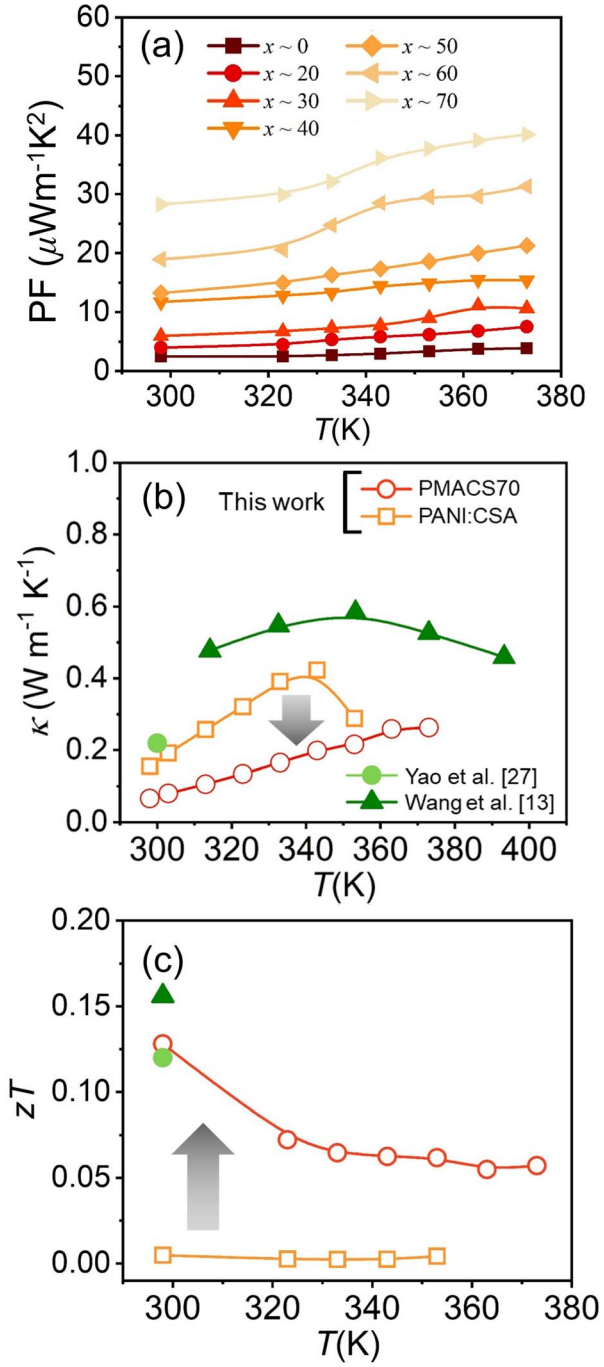

Fig. 6 Temperature dependent (a) power factor for PMACS (0–70 wt%), (b) thermal conductivity (κ) and (c) thermoelectric figure of merit (zT) value for PANI:CSA and PMACS70. Previously reported values from Yao *et al.*[27] and Wang *et al.*[13] are included for comparison.

attributed to the decreased thermal conductivity at ~300 K. Analysis of the thermal transport indicates that the increase in $\kappa(T)$ with temperature is strongly correlated with an increase in heat capacity, likely due to increased molecular mobility, additional vibrational modes, or structural changes within the PANI polymer matrix, such as enhanced segmental motion or increased amorphous content.

The calculated zT for PANI:CSA and PMACS70 is shown in Fig. 6(c). Pristine PANI exhibits a low zT (~0.004–0.02) primarily due to a very low Seebeck coefficient. However, nanocomposite formation (PMACS70) leads to a marked improvement, with zT values increasing to ~0.13. The observed degradation in zT with temperature is governed primarily by an increase in $\kappa(T)$ associated with enhanced heat capacity, rather than by any deterioration in electronic transport properties. A detailed comparison with state-of-the-art PANI-based composites is provided in the SI (Section S5, Table S3). The synthesized PMACS shows comparable zT to graphene–PANI, PANI/SWCNT, and PANI/Te composites, which typically exhibit power factors of ~80–120 μW m^{-1} K^{-2} at 300 K due to conductive networks or chalcogenide interfaces. This performance arises from an enhanced Seebeck coefficient and power factors, with synergistic κ reduction. Further improvements are possible through morphology control and optimized conductive network or multilayer design.

2.9 Carrier-energy-dependent transport modeling: semi-localized transport (SLoT) framework

In PANI nanocomposites, energy filtering arises from interfaces or barriers that selectively transmit high-energy carriers. By combining transport measurements (σ, S, and T) with Kang–Snyder[31] and SLoT[32] modeling, one can quantitatively validate the charge carrier localization and scattering based energy filtering effect to describe the transport in conjugated polymers, by analyzing the carrier energy-dependent transport. The Kang–Snyder framework[31] (described in SI S7.2) provides a semi-empirical approach to describe thermoelectric transport. This invariance of $s \approx 1$ across the composition demonstrates that incorporation of MACS does not alter the fundamental scattering mechanism, which remains characteristic of diffusive polaron transport in conducting polymers as shown in Fig. S18. Together with the KS formalism, SLoT[32] provides a comprehensive description of transport in PMACS composites, as shown in Fig. 7(a) and (b), with the $S-\sigma$ plots at 297 K and full temperature range, respectively, where enhanced interfacial connectivity (increased σ_{E0}) and moderate effective carrier localization (increased W_H) coexist to yield an optimized balance between thermopower and conductivity.

The data collapsing onto the same parabola indicates that charge transport in all samples is governed by the same underlying polaronic or bipolaronic conduction mechanism. The green shaded region is referred to as spatial localization, which considers the effects of localization in a disordered polymer. However, the absolute values shift at higher MACS towards the KS regime, which may be due to increased interfacial connectivity (transport coefficient, σ_{E0}) and reduced chemical potential, which suggests the existence of energy filtering of low energy polarons as also have been observed in XPS, and trends of Hall measurements (increased mobility and decreased conductivity). The fact that all temperature-dependent data fit a single parabola implies that the scattering parameter (s) remains constant across samples, while only the transport coefficient term (σ_0) varies, reflecting

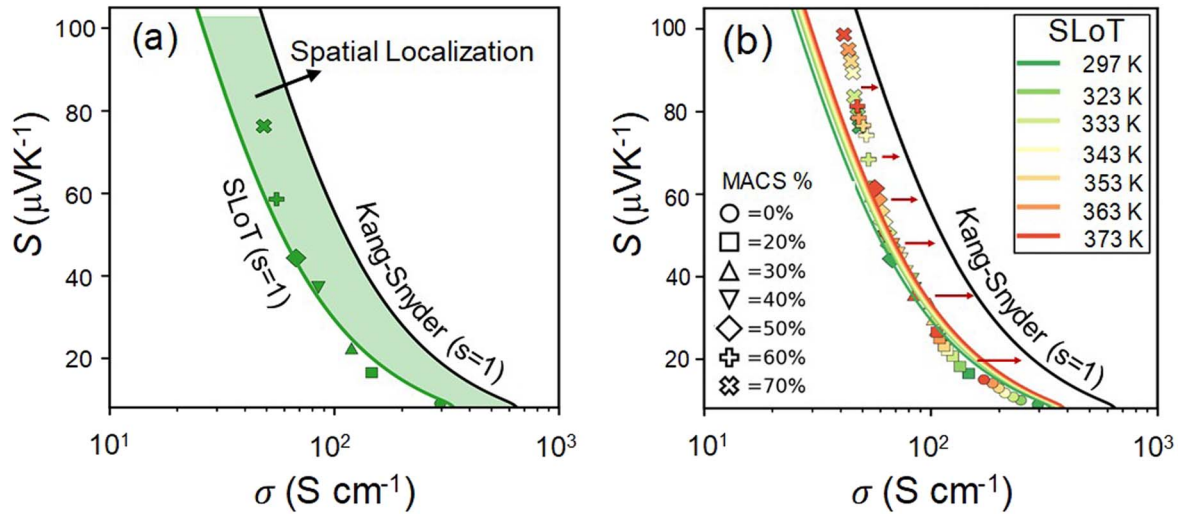

Fig. 7 Comparison of Kang–Snyder and Semi-Localized Transport (SLoT) models for PMACS composites. (a) S–σ correlation at 297 K showing the SLoT fit (green) with a spatial-localization envelope relative to the Kang–Snyder baseline ($s = 1$). (b) Temperature-dependent SLoT family (297–373 K) illustrating the leftward shift of the experimental data from the SLoT model to the Kang–Snyder curve at higher MACS contents due to energy-dependent scattering of charge carriers realizing the energy filtering effect.

differences in morphology, doping level, and filler-induced microstructure. In Fig. 7(b), the data points are shifting from the SLoT curve to the right (KS-curve), which may be due to increased interfacial effects or a percolated structure which may enhance the interconnectivity at the interfaces scattering the low energy carriers. So, recalling the Hall results, we assume that enhanced mobility may also be due to this good interconnectivity at the interfaces which can scatter the low energy carriers. Therefore, apart from charge carrier localization, there may also be scattering based energy filtering of the charge carriers that is resulting in an enhanced Seebeck coefficient.

Arrhenius-type linear fits (Fig. S22) yield W_H values that increase from nearly zero for pristine PANI:CSA to ≈20 meV for intermediate loadings and up to ≈30 meV for 60–70 wt% MACS, as shown in Fig. 8(a). The non-monotonic variation, with a shallow minimum near 40 wt% indicates that moderate inorganic incorporation enhances interchain connectivity while excessive loading introduces deep interfacial traps and localized potential fluctuations. Fig. 8(b) further correlates σ_{E0} with the reduced chemical potential (η), showing a monotonic increase of σ_{E0} with lowering η across MACS compositions, indicating improved interchain connectivity and effective

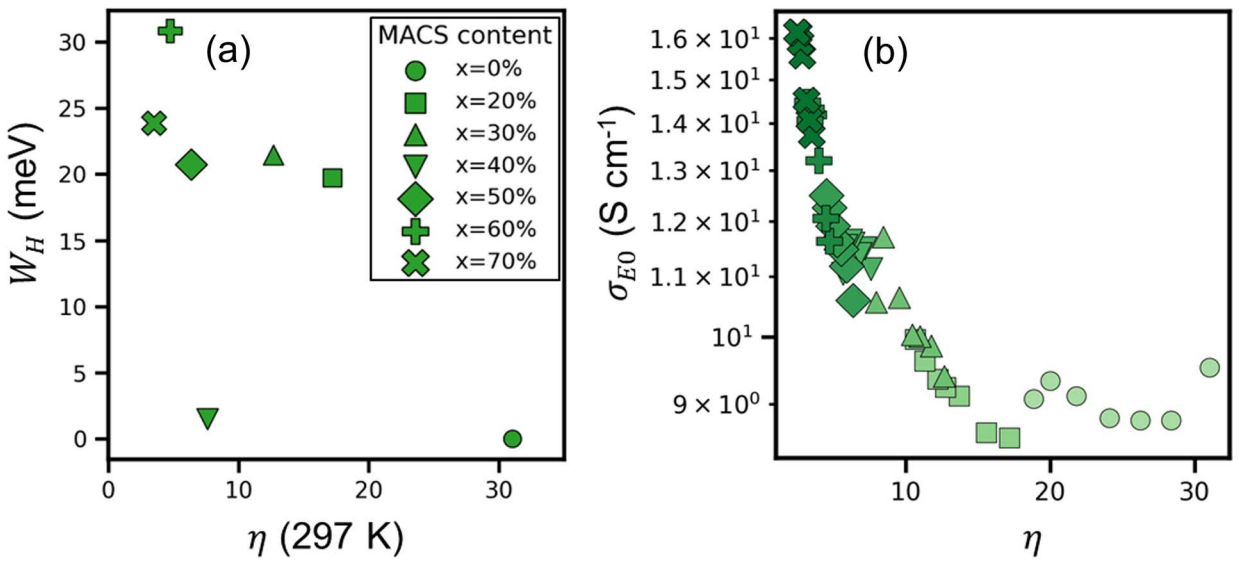

Fig. 8 Correlation of effective localization energy and reduced chemical potential from SLoT analysis of PANI:CSA/MACS composites. (a) Variation of the effective localization energy barrier (W_H) with reduced chemical potential (η) showing increased carrier localization/filtering at lower η (higher MACS). (b) Relationship between the reduced transport coefficient (σ_{E0}) and η, indicating enhanced percolative connectivity and carrier transport efficiency with increasing η.

charge percolation, before saturating due to the onset of interfacial localization and trap formation. These localized states originate from structural disorder and charge confinement at the PANI/MACS interface, consistent with the Raman and XPS evidence of polaron suppression and bipolaron stabilization. In other words, we can say that increasing effective localization energy means that the charges are being localized due to energetic disorder in the polymer system introduced by the inorganic filler. But with increasing filler, the interconnectivity/percolation is also increased which means diffusive transport is taking place where low energy carriers are being scattered. So, W_H not only quantifies the strength of localization but also connects microscopically to energy filtering effects at polymer–inorganic interfaces. The offset in electronic energy levels between PANI and MACS introduces shallow interfacial potential barriers that preferentially scatter low-energy carriers, thereby increasing the Seebeck coefficient while simultaneously reducing electrical conductivity. The SLoT model thus unifies both effects within a single thermally activated framework: the exponential damping term encapsulates localized hopping and energy filtering, whereas the Fermi-integral statistics preserve the intrinsic Seebeck response of the conducting polymer. By unifying the KS and SLoT model observations, this study aims to bridge empirical polymer-inorganic transport observations with quantitative energy-dependent carrier statistics. The invariant s and tunable W_H parameters together provide a concise metric to evaluate connectivity-localization balance in hybrid thermoelectrics.

2.10 Flexible thermoelectric generator (FTEG) for wearable applications

The thermoelectric performance of the flexible PANI:CSA/70 wt% MACS nanocomposite device was systematically examined to evaluate its voltage response, structural configuration, and practical heat-harvesting capability. Fig. 9(a) shows the measured output voltage (V_o) as a function of the temperature difference (ΔT) across the device, where the inset shows the schematics of the device illustrating the configuration of alternating PANI:CSA/70 wt% MACS nanocomposite films patterned on a Kapton substrate, providing both flexibility and mechanical robustness. The alternate arrangement of p-type thermoelectric elements ensures a cumulative voltage generation under a temperature gradient, while the Kapton substrate maintains stable performance under bending and thermal

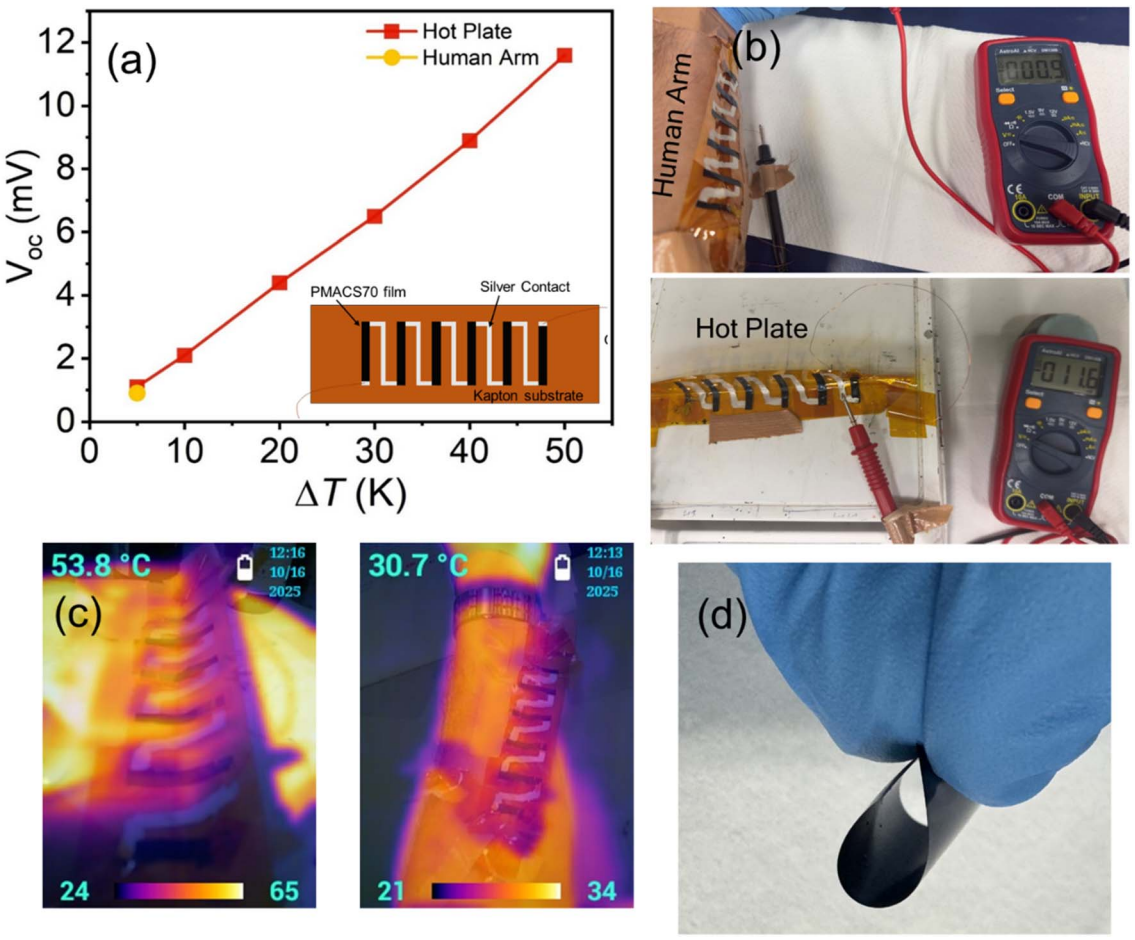

Fig. 9 (a) Output voltage (V_o) *versus* ΔT confirming the thermoelectric response; inset: device schematic on a Kapton substrate with alternating PANI:CSA/70 wt% MACS nanocomposite flexible films, (b) on-body heat harvesting demonstration from the human arm and ΔT induced by a hot plate, (c) thermal images showing the generated temperature gradient, and (d) photograph illustrating film flexibility.

cycling. A linear increase in V_o with ΔT confirms a reliable thermoelectric response, demonstrating the effective charge carrier transport within the hybrid films. The slope of the V_o–ΔT plot corresponds to the Seebeck coefficient, validating the material's intrinsic potential for low-grade heat conversion.

To demonstrate real-world applicability, the on-body heat harvesting test (Fig. 9(b)) was performed by placing the device on a human arm, where the temperature difference between skin and ambient air generated a measurable output voltage, V_{OC} ~0.9 mV. A similar test on a controlled hot-plate setup produced a comparable thermoelectric response (V_{OC} ~11.6 mV at $\Delta T = 50$ K), confirming reproducibility under variable ΔT conditions. Infrared thermal images (Fig. 9(c)) captured during operation clearly show the established temperature gradient (ΔT) across the flexible film segments, validating the uniform heat distribution and effective thermal coupling between the substrate and the active thermoelectric regions. As shown in Fig. 9(d), the device maintains its integrity and electrical output even under repeated bending and twisting, demonstrating excellent mechanical flexibility (the flexibility test is also demonstrated in Fig. S13). The robust polymer–inorganic hybrid structure ensures consistent thermoelectric performance suitable for wearable and conformal energy-harvesting applications.

3 Conclusion

PANI:CSA/MACS-based polymer nanocomposites were designed to systematically optimize their electronic properties and thermoelectric performance through combined interfacial energy filtering and charge localization. The polymer chain conformation and uniform MACS dispersion were carefully controlled to regulate charge-transport pathways, while incorporation of the inorganic MACS phase within the PANI matrix introduced energy filtering and charge-carrier localization effects that enhanced the Seebeck coefficient and power factor. The composites exhibit S increasing from ~10–75 μV K^{-1}, and a decreasing σ from ~298 – 50 S cm^{-1} with increasing MACS loading at room temperature, yielding a power factor of ~28 μW m^{-1} K^{-2}. For PANI/MACS 70 wt%, the Seebeck coefficient reaches ~99 μV K^{-1} at ~373 K, with a high PF of ~40 μW m^{-1} K^{-2}. The thermal conductivity in PMACS70 is reduced to ~0.06 W m^{-1} K^{-1} at ~300 K, with a corresponding high zT value of ~0.13. Quantitative analysis using the Kang–Snyder framework confirms an invariant scattering parameter ($s = 1$), indicating preserved diffusive polaronic transport, while the SLoT model introduces a localization energy (W_H) that quantifies the degree of carrier localization. The evolution from a SLoT-governed semi-localized regime at low filler loadings to a shift to a KS-dominated regime at higher loadings evidences the transition from disorder-limited to interfacial diffusive transport, providing a mechanistic explanation for the partial decoupling of the S–σ trade-off and highlighting controlled disorder and interfacial engineering as effective design strategies. Rietveld refinement indicates the preservation of the pseudo-orthorhombic framework with anisotropic structural adaptation upon hybridization. Variations in the electron density function across the polymer unit cell with different inorganic fillers underscore the coupled effects of chain alignment and interfacial charge transfer, resulting in anisotropic structural response in PANI-based hybrids. Raman and XPS analyses reveal conformational reorganization and electronic coupling at the polymer–filler interface, while UV-vis-NIR spectra confirm de-doping-induced charge localization. Collectively, these findings demonstrate a structurally robust polymer–inorganic network that sustains stable thermoelectric performance, suitable for flexible and wearable energy-harvesting devices.

Author contributions

Anmol Sharma: writing – original daft, investigation, methodology, conceptualization, writing – review & editing. Nagendra Singh Chauhan: writing – review & editing, writing – original draft, supervision, methodology, conceptualization. Takao Mori: writing – review & editing, supervision, project administration, methodology, funding acquisition, conceptualization.

Conflicts of interest

There is no conflict of interest to declare.

Data availability

The data that support the findings of this study are available upon request from the authors.

Supplementary information (SI): experimental procedures for PANI:CSA/MACS hybrid film fabrication and characterization methods. Additional data include structural parameters, crystallographic details, and SEM micrographs. See DOI: https://doi.org/10.1039/d5ta09036a.

Acknowledgements

This achievement was supported by JST SPRING, Grant Number JPMJSP2124. The authors gratefully acknowledge financial support from the JST Mirai Program, Japan (Grant No. JPMJMI19A1).

References

1 N. Nandihalli, C.-J. Liu and T. Mori, *Nano Energy*, 2020, **78**, 105186.
2 T. Mori and S. Priya, *MRS Bull.*, 2018, **43**, 176.
3 G. Prunet, F. Pawula, G. Fleury, E. Cloutet, A. J. Robinson, G. Hadziioannou and A. Pakdel, *Mater. Today Phys.*, 2021, **18**, 100402.
4 H. S. Kim, W. Liu, G. Chen, C.-W. Chu and Z. Ren, *Proc. Natl. Acad. Sci. U. S. A.*, 2015, **112**, 8205.
5 M. Bharti, A. Singh, S. Samanta and D. K. Aswal, *Prog. Mater. Sci.*, 2018, **93**, 270.
6 H. Wang and C. Yu, *Joule*, 2019, **3**, 53.
7 Y. Wang, R. Chetty, Z. Liu, L. Wang, T. Ohsawa, W. Gao and T. Mori, *J. Mater. Chem. C*, 2022, **10**, 12610.
8 P. Colomban, S. Folch and A. Gruger, *Macromolecules*, 1999, **32**, 3080.

9 M. Cochet, G. Louarn, S. Quillard, J. P. Buisson and S. Lefrant, *J. Raman Spectrosc.*, 2000, **31**, 1041.
10 M. Pope and C. E. Swenberg, *Electronic Processes in Organic Crystals and Polymers*, Oxford University Press New York, NY, 2nd edn, 1999.
11 T. Cao, X.-L. Shi, J. Zou and Z.-G. Chen, *Microstructures*, 2021, **1**, 1–33.
12 J. Li, A. B. Huckleby and M. Zhang, *J. Mater.*, 2022, **8**, 204.
13 Y. Wang, S. M. Zhang and Y. Deng, *J. Mater. Chem. A*, 2016, **4**, 3554.
14 K. Chatterjee, M. Mitra, K. Kargupta, S. Ganguly and D. Banerjee, *Nanotechnology*, 2013, **24**, 215703.
15 C. Guo, F. Chu, P. Chen, J. Zhu, H. Wang, L. Wang, Y. Fan and W. Jiang, *J. Mater. Sci.*, 2018, **53**, 6752.
16 H. Ju, D. Park and J. Kim, *ACS Appl. Mater. Interfaces*, 2018, **10**, 11920.
17 O. Zapata-Arteaga, S. Marina, G. Zuo, K. Xu, B. Dörling, L. A. Pérez, J. S. Reparaz, J. Martín, M. Kemerink and M. Campoy-Quiles, *Adv. Energy Mater.*, 2022, **12**, 2104076.
18 V. Vijayakumar, Y. Zhong, V. Untilova, M. Bahri, L. Herrmann, L. Biniek, N. Leclerc and M. Brinkmann, *Adv. Energy Mater.*, 2019, **9**, 1900266.
19 Y. Wang, C. Yu, M. Sheng, S. Song and Y. Deng, *Adv. Mater. Interfaces*, 2018, **5**, 1701168.
20 L. Wang, Q. Yao, W. Shi, S. Qu and L. Chen, *Mater. Chem. Front.*, 2017, **1**, 741.
21 F. Erden, H. Li, X. Wang, F. Wang and C. He, *Phys. Chem. Chem. Phys.*, 2018, **20**, 9411.
22 A. S. Kshirsagar, P. V. More, A. Dey and P. K. Khanna, *Dalton Trans.*, 2019, **48**, 14497.
23 H. Li, Y. Liu, P. Li, S. Liu, F. Du and C. He, *ACS Appl. Mater. Interfaces*, 2021, **13**, 6650.
24 H. Li, Y. Liang, S. Liu, F. Qiao, P. Li and C. He, *Org. Electron.*, 2019, **69**, 62.
25 H. Wang, S. Yi, X. Pu and C. Yu, *ACS Appl. Mater. Interfaces*, 2015, **7**, 9589.
26 C. Gayner and Y. Amouyal, *Adv. Funct. Mater.*, 2020, **30**, 1901789.
27 Q. Yao, Q. Wang, L. Wang and L. Chen, *Energy Environ. Sci.*, 2014, **7**, 3801.
28 A. Sharma, N. S. Chauhan, M. Nishimagi and T. Mori, *Mater. Today Phys.*, 2025, **57**, 101794.
29 S. Y. Back, S. Meikle and T. Mori, *J. Mater. Sci. Technol.*, 2025, **227**, 57.
30 Z. Liu, N. Sato, W. Gao, K. Yubuta, N. Kawamoto, M. Mitome, K. Kurashima, Y. Owada, K. Nagase, C.-H. Lee, J. Yi, K. Tsuchiya and T. Mori, *Joule*, 2021, **5**, 1196.
31 S. D. Kang and G. J. Snyder, *Nat. Mater.*, 2017, **16**, 252.
32 S. A. Gregory, R. Hanus, A. Atassi, J. M. Rinehart, J. P. Wooding, A. K. Menon, M. D. Losego, G. J. Snyder and S. K. Yee, *Nat. Mater.*, 2021, **20**, 1414.
33 J. P. Pouget, M. E. Jozefowicz, A. J. Epstein, X. Tang and A. G. MacDiarmid, *Macromolecules*, 1991, **24**, 779.
34 Z. Liu, N. Sato, W. Gao, K. Yubuta, N. Kawamoto, M. Mitome, K. Kurashima, Y. Owada, K. Nagase, C.-H. Lee, J. Yi, K. Tsuchiya and T. Mori, *Joule*, 2021, **5**, 1196.
35 E. A. Sanches, A. D. S. Carolino, A. L. D. Santos, E. G. R. Fernandes, D. M. Trichês and Y. P. Mascarenhas, *Adv. Mater. Sci. Eng.*, 2015, **1**, 375312.
36 D. Djurado, Y. Nicolau, I. Dalsegg and E. Samuelsen, *Synth. Met.*, 1997, **84**, 121.
37 F. Roussel, R. Chen Yu King, M. Kuriakose, M. Depriester, A. Hadj-Sahraoui, C. Gors, A. Addad and J.-F. Brun, *Synth. Met.*, 2015, **199**, 196.
38 G. M. Do Nascimento and M. L. A. Temperini, *J. Raman Spectrosc.*, 2008, **39**, 772.
39 Z. Morávková and P. Bober, *Int. J. Polym. Sci.*, 2018, **2018**, 1.
40 M.-I. Boyer, S. Quillard, E. Rebourt, G. Louarn, J. P. Buisson, A. Monkman and S. Lefrant, *J. Phys. Chem. B*, 1998, **102**, 7382.
41 S. Quillard, G. Louarn, J. P. Buisson, S. Lefrant, J. Masters and A. G. MacDiarmid, *Synth. Met.*, 1993, **55**, 475.
42 T. Lindfors and A. Ivaska, *J. Electroanal. Chem.*, 2005, **580**, 320.
43 J. E. P. D. Silva, S. I. C. D. Torresi and M. L. A. Temperini, *J. Braz. Chem. Soc.*, 2000, **11**, 91.
44 R. Mažeikienė, G. Niaura and A. Malinauskas, *Electrochem. Commun.*, 2005, **7**, 1021.
45 G. M. Do Nascimento, V. R. L. Constantino, R. Landers and M. L. A. Temperini, *Macromolecules*, 2004, **37**, 9373.
46 M. Tagowska, B. Pałys and K. Jackowska, *Synth. Met.*, 2004, **142**, 223.
47 G. M. Do Nascimento, P. Y. G. Kobata, R. P. Millen and M. L. A. Temperini, *Synth. Met.*, 2007, **157**, 247.
48 G. Niaura, R. Mažeikien≐ and A. Malinauskas, *Synth. Met.*, 2004, **145**, 105.
49 M. Kim, D. Park and J. Kim, *Polymers*, 2021, **13**, 1518.
50 Y. Zhao, G.-S. Tang, Z.-Z. Yu and J.-S. Qi, *Carbon*, 2012, **50**, 3064.
51 D. Ji, B. Li, B. T. Raj, X. Li, D. Zhang, M. Rezeq, W. Cantwell and L. Zheng, *Adv. Mater. Interfaces*, 2025, **12**, 2400566.
52 L. Wang, Q. Yao, H. Bi, F. Huang, Q. Wang and L. Chen, *J. Mater. Chem. A*, 2015, **3**, 7086.
53 P. Zhang, X. Zhai, H. Huang, J. Zhou, X. Li, Y. He and Z. Guo, *J. Mater. Sci.: Mater. Electron.*, 2020, **31**, 14625.
54 O. A. Abdulrazzaq, S. E. Bourdo, V. Saini and A. S. Biris, *J. Mater. Sci.: Mater. Electron.*, 2020, **31**, 21640.
55 B. J. Waghmode, R. Soni, K. R. Patil and D. D. Malkhede, *New J. Chem.*, 2017, **41**, 9752.
56 S. Golczak, A. Kanciurzewska, M. Fahlman, K. Langer and J. Langer, *Solid State Ionics*, 2008, **179**, 2234.
57 X.-L. Wei, M. Fahlman and A. J. Epstein, *Macromolecules*, 1999, **32**, 3114.
58 Q. Zou, H. Shang, L. Zhang, C. Feng, H. Gu and F. Ding, *Appl. Surf. Sci.*, 2023, **638**, 158100.
59 *Handbook of X-Ray Photoelectron Spectroscopy: a Reference Book of Standard Spectra for Identification and Interpretation of XPS Data, Update*, ed. J. F. Moulder and J. Chastain, Perkin-Elmer Corporation, Eden Prairie, Minn, 1992.
60 M. C. Biesinger, B. P. Payne, A. P. Grosvenor, L. W. M. Lau, A. R. Gerson and R. St. C. Smart, *Appl. Surf. Sci.*, 2011, **257**, 2717.

61 H. Li, Y. Liang, Y. Liu, S. Liu, P. Li and C. He, *Compos. Sci. Technol.*, 2021, **210**, 108797.
62 V. Ugraskan and F. Karaman, *J. Electron. Mater.*, 2021, **50**, 3455.
63 *Nanostructured Conductive Polymers*, ed. A. Eftekhari, Wiley, Chichester, West Sussex, U.K Hoboken, N.J, 2010.
64 Y. P. A. Manasa, R. Shankar, A. N. Prabhu, R. Nayak, A. Rao and G. Poojitha, *RSC Adv.*, 2024, **14**, 40117.
65 K.-H. Lee, B. J. Park, D. H. Song, I.-J. Chin and H. J. Choi, *Polymer*, 2009, **50**, 4372.
66 L. W. Shacklette, *Synth. Met.*, 1994, **65**, 123.
67 Q. Yao, Q. Wang, L. Wang, Y. Wang, J. Sun, H. Zeng, Z. Jin, X. Huang and L. Chen, *J. Mater. Chem. A*, 2014, **2**, 2634.
68 A. G. MacDiarmid and A. J. Epstein, *Synth. Met.*, 1995, **69**, 85.
69 A. G. MacDiarmid and A. J. Epstein, *Synth. Met.*, 1994, **65**, 103.
70 H. Yan, T. Ohta and N. Toshima, *Macromol. Mater. Eng.*, 2001, **286**, 139.
71 M. Singh, A. K. Gautam, M. Faraz and N. Khare, *ACS Appl. Energy Mater.*, 2024, **7**, 133.
72 M. Singh, A. K. Gautam, M. Faraz and N. Khare, *Eur. Phys. J. Plus*, 2022, **137**, 1251.
73 K. Lee, S. Cho, S. Heum Park, A. J. Heeger, C.-W. Lee and S.-H. Lee, *Nature*, 2006, **441**, 65.
74 Y. Long, L. Zhang, Z. Chen, K. Huang, Y. Yang, H. Xiao, M. Wan, A. Jin and C. Gu, *Phys. Rev. B*, 2005, **71**, 165412.
75 Z. H. Wang, A. Ray, A. G. MacDiarmid and A. J. Epstein, *Phys. Rev. B*, 1991, **43**, 4373.
76 J. Joo, S. M. Long, J. P. Pouget, E. J. Oh, A. G. MacDiarmid and A. J. Epstein, *Phys. Rev. B*, 1998, **57**, 9567.
77 A. L. Efros and M. Pollak, *Electron-Electron Interactions In Disordered Systems*, Elsevier, 2012, vol. 10.
78 S. Shekhar, V. Prasad and S. V. Subramanyam, *Phys. Lett. A*, 2006, **360**, 390.
79 S. Watanabe, M. Ohno, Y. Yamashita, T. Terashige, H. Okamoto and J. Takeya, *Phys. Rev. B*, 2019, **100**, 241201.